Modeling and Analysis of a Differential Mode Active EMI Filter With an Analog Twin Circuit

Balaji Narayanasamy , *Member, IEEE*, Hongwu Peng , *Graduate Student Member, IEEE*, Zhao Yuan , Asif Imran Emon , *Graduate Student Member, IEEE*, and Fang Luo

Abstract-Conventional passive EMI filters are bulky and occupy up to 30% of converter volume and weight. Active EMI filters are a key technology that enables the volume reduction of passive components in the EMI filter. The effectiveness of traditional active EMI filter for volume reduction is limited by the additional overhead from the passive components for noise sensing and compensation to ensure stability. In this article, a novel active EMI filter is proposed and demonstrated for differential mode noise attenuation. The filter consists of a twin circuit made up of low voltage/current components that mimic the high-power passive filter components in the main circuit. Unlike the conventional active EMI filter, the proposed filter uses compensation networks which consists of low-voltage surface-mount components only. The modeling of the entire circuit is carried out, and verified with small-signal measurements. The filter is then tested in a converter and the experimental results are shown to be consistent with the model and the small-signal measurements.

Index Terms—Active EMI filters, analog twin circuit, conducted emissions, passive EMI filters.

I. INTRODUCTION

OWER converters generate EMI noise due to the switching action of the power semiconductor devices. Conventionally, a second-order passive EMI filter is used for noise mitigation to ensure compliance with standards. With the advent of wide-bandgap devices such as SiC and GaN, the power density of the power stages is ever increasing, as demonstrated in the literature [1]–[5]. While the power density of the power stage increases, the high switching frequency and high switching speeds of the wide-bandgap devices introduces more challenges [6], [7] require careful design of EMI filters to ensure the high power density of the entire power converter. However, the passive components have not kept up with the developments in the power semiconductors area. Therefore, passive EMI filters

Manuscript received December 29, 2019; revised May 27, 2020; accepted June 24, 2020. Date of publication July 13, 2020; date of current version August 13, 2020. This work was supported by the National Science Foundation (NSF) under Award 1846917. This article was presented in part at the 2019 IEEE International Symposium on Electomagnetic Compatibility, Signal and Power Integrity, New Orleans, LA, USA, July 2019. (Corresponding author: Balaji Narayanasamy.)

The authors are with the Department of Electrical Engineering, University of Arkansas, Fayetteville, AR 72701 USA (e-mail: bnarayan@uark.edu; hp013@uark.edu; zhaoyuan@uark.edu; aiemon@uark.edu; fangluo@ieee.org, kkhust@gmail.com).

Color versions of one or more of the figures in this article are available online at https://ieeexplore.ieee.org.

Digital Object Identifier 10.1109/TEMC.2020.3006427

are a significant bottleneck for power density and could occupy up to 30% of power converter volume and weight.

Active EMI filters are a key technology that will enable high-density passive solutions for the next generation of power converters. Typically, active EMI filters are implemented along with another passive component. This is essential because of the limitation of the bandwidth of the passive components and the active circuits used in the active EMI filter. Using active EMI filters along with a passive component is referred to as hybrid EMI filters. Active and hybrid EMI filters have been shown to reduce the volume of the passive components by over 50% [8]-[10]. The active EMI filters provide attenuation up to a few MHz, and a smaller passive filter is used to provide high-frequency attenuation. The active EMI filters can be classified based on the methodology of control, noise sensing, and noise-cancellation mechanisms [11]-[13]. Previously, active EMI filters using feedforward [11], feedback [10], [14], [15], and a combination of both control techniques [16] have been demonstrated. Also, active EMI filters utilizing a combination of voltage or current sensing and cancellation have been demonstrated [8], [9], [17]–[19]. Active and hybrid EMI filters have been applied to common mode (CM) and differential mode (DM) noise attenuation in both dc-dc [9], [20], ac-dc [10], [14], [17], and dc–ac [11], [21] converters.

Among existing work, transformerless current-cancellation topologies have been shown to offer higher volume reductions than voltage-cancellation topologies that use a voltage injector. Recently, a summary of different active EMI filters and their implementation of different power converters was presented in [22]. In [22], the need for novel analog or digital active EMI filters with improved performance (attenuation) while avoiding additional passive components for compensation was identified. In order to get good attenuation with the feedforward topology, tight control of tolerance of all the passive components is required. Moreover, for the most part, the feedforward topology remains stable.

While the feedback topology is resilient to component tolerances, it is subject to stability issues at low (<150 kHz) and high (>30 MHz) frequencies. Instability at low frequency occurs due to the phase shift introduced by the noise-sensing circuit. High frequency instability stems from the gain roll-off of the op-amp circuit, and other parasitics in the circuit. In order to ensure stability, damping networks comprising of high-voltage/high-current components are added to the circuit. These components add to the bulk and reduce the benefits of

0018-9375 © 2020 IEEE. Personal use is permitted, but republication/redistribution requires IEEE permission. See https://www.ieee.org/publications/rights/index.html for more information.

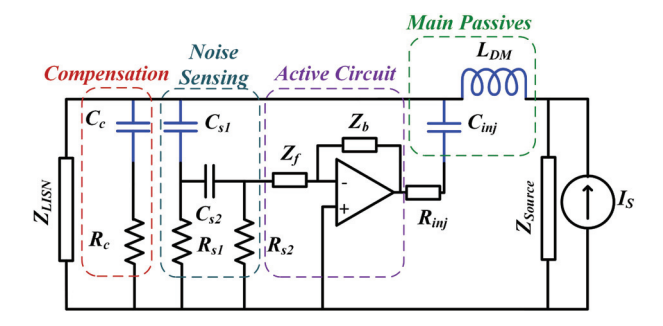


Fig. 1. Schematic of typical feedback control based voltage-sense currentcancellation active EMI filter.

using active EMI filters. The schematic of a typical feedback control based voltage-sense current-cancellation active EMI filter is shown in Fig. 1. There are four main parts of the active EMI filter. They are: the noise-sensing circuit, the active circuit (op-amp), the main passives, and the compensation network. In [15], attenuation of up to 34 dB around 150 kHz in an ac-dc converter with PFC using feedback current-sense current-cancellation topology active EMI filter was reported. However, in addition to the current transformer (CT) for noise sensing, additional high-voltage capacitor (C_C) and resistor (R_C) compensation network to ensure the stability of the active EMI filter. This additional high-voltage compensation network prevents maximizing the volumetric benefit of using an active EMI filter. It was shown in [14] that for an ac-dc converter without PFC, voltage-sense current-cancellation active EMI filter offers the most volume reduction. While this method avoided any CTs and additional high-voltage compensation network, an attenuation of only 12 dB was achieved around 150 kHz. The main bottleneck that limits the performance was identified as the phase shift introduced by the noise sensing second-order high-pass filter.

This work proposes a novel active EMI filter with a twin circuit. The proposed active EMI filter overcomes the stability issues facing a conventional feedback control based implementation. The proposed topology does not require any high voltage/current components for compensation, and instead only uses low-voltage surface mount components. Some of the preliminary results in this article were previously presented by the authors in [23]. The rest of this article is organized as follows. Section II describes the proposed concept of the active EMI filter with a twin circuit. Section III involves the modeling, design, and frequency domain measurements using the VNA to verify the modeling of individual subcircuits and insertion loss of the entire filter as a whole. Section IV describes the experimental test setup, and discusses the small signal and experimental results. Finally, Section V presents the conclusion.

II. ACTIVE EMI FILTER WITH TWIN CIRCUIT

A. Topology Selection of Active EMI Filter

The active EMI filter could use either noise current or noise voltage sensing and cancellation. Topologies that employ current-sensing and voltage-cancellation requires the use of CTs for current-sensing and voltage-injection transformers

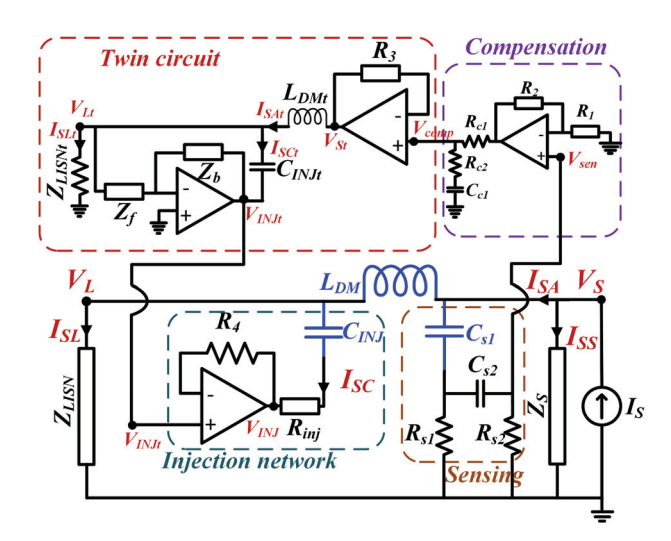


Fig. 2. Schematic of proposed feedforward control based voltage-sense current-cancellation active EMI filter with twin circuit.

for voltage injection, respectively. For DM noise, the CTs and voltage injection transformers can be bulky since they have to carry the line current without getting saturated. Therefore, using these topologies would affect volume reduction benefits that come with the use of the active EMI filter. Therefore, it is more desirable to use active EMI filter topologies that do not require the use of any additional magnetic components. The voltage-sense current-cancellation topology uses only high voltage capacitors in combination with low voltage active circuits for noise sensing and cancellation. Therefore, using this topology will help maximize the volume reduction and therefore, is used in this article. Previously, feedback control based voltage-sense current-cancellation topology was demonstrated in [14]. However, in order to avoid using additional high-voltage components for compensation for stability improvement, the attenuation of the active EMI filter was limited to 12 dB around 150 kHz. This work proposes a topology that only uses low-voltage components for compensation but still implements voltage-sense current-cancellation active EMI filter for DM noise cancellation while achieving 24 dB attenuation around 150 kHz.

B. Feedforward Voltage-Sense Current-Cancellation Active EMI Filter With Twin Circuit

The schematic of the overall implementation of the proposed active EMI filter for DM noise attenuation is shown in Fig. 2. The converter is represented by the current source, I_S , and the noise source impedance Z_S represents the impedance of the dc-link capacitor. The load impedance $Z_{\rm LISN}$ represents the equivalent impedance of the LISN for DM noise. The original passive EMI filter consists of inductance, $L_{\rm DM}$, and capacitor, $C_{\rm DM}$. The proposed active EMI filter enhances the impedance of $C_{\rm DM}$. And, in combination with $L_{\rm DM}$, it forms the hybrid EMI filter. This $L_{\rm DM}$ could be a discrete inductor or leakage inductance of the CM choke. In the active EMI filter, the $C_{\rm DM}$ is referred to as the $C_{\rm INJ}$ since the noise current is injected through this capacitor. Noise sensing is carried out at the converter end, making this implementation a feedforward topology.

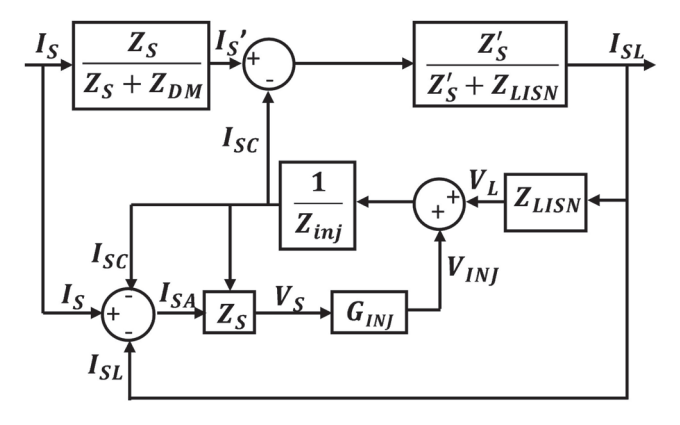


Fig. 3. Block diagram of proposed active EMI filter—twin circuit block diagram collapsed into G_{INJ} .

There are four parts of the proposed active EMI filter circuit. The first stage involves the noise sensing high-pass filter. It consists of a second-order high-pass filter that rejects any line frequency and other harmonics and senses only the switching frequency and its harmonics. The second stage is the compensation stage. The output of the high-pass filter is buffered, and the compensation network is used to improve the gain and phase around 150 kHz (start of EMI frequency range). The compensation network uses only low-voltage components and is key to enhance the attenuation of the active EMI filter. The next stage is the twin circuit. The output of the compensation network is fed to the twin circuit that comprises of the components that mirror the main filter components. That is, corresponding to $L_{\rm DM}$, $C_{\rm INJ}$, and $Z_{\rm LISN}$ in the main power circuit; there are $L_{\rm DMt}$, $C_{\rm INJt}$, and $Z_{\rm LISNt}$ in the twin circuit. The twin circuit consists of a feedback control based voltage-sense current-cancellation topology active EMI filter. All the components in the twin circuit are low-voltage and low-power components. The final stage is the noise injection stage. This circuit buffers the injected noise in the twin circuit, V_{INJt} , and injects into the main circuit. Ideally, all the active circuitry and its components of the active circuit with the exception of $L_{\rm DMt}$ and $C_{\rm INJt}$ could be integrated into a single IC. Even then, since these components do not carry the line current or do not have to block the line voltage, they can be made from surface mount components or much smaller in volume relative to passive components in the power circuit for all cases. Moreover, the filter would be more beneficial at higher power levels. Furthermore, in the entire active EMI filter, there are only two high-voltage components – C_{S1} and C_{INJ} capacitors avoiding the need for additional magnetic components or high-voltage capacitors.

III. MODELING OF THE ACTIVE EMI FILTER AND TWIN CIRCUIT

The block diagram of the entire active EMI filter circuit is shown in Fig. 3, and the equivalent circuit is shown in Fig. 4(a). I_{SS} is the current through Z_S , and I_{SA} represents the current flowing through the filter. This cancellation current injected by the filter and the noise current through the LISN is represented by I_{SC} and I_{SL} , respectively. Alternatively, the DM noise source

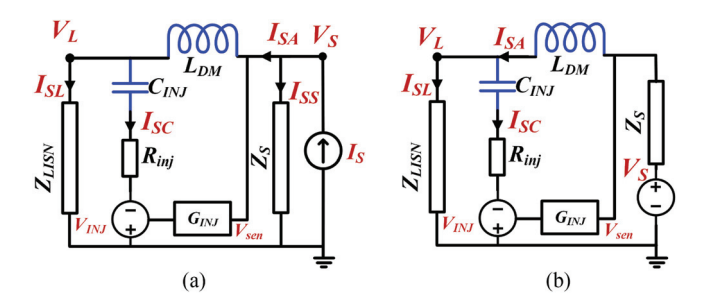


Fig. 4. (a) Equivalent circuit of proposed active EMI filter with noise source represented by current source. (b) Noise source represented by voltage source.

could be represented by the voltage source V_S given by (1) in series with an impedance, as shown in Fig. 4(b). Now, the sensed voltage, $V_{\rm SEN}$ is given by (2). Combining the impedance of $L_{\rm DM}$, $Z_{\rm DM}$, and noise-source impedance, Z_S , simplifies the derivation of the open-loop current gain. The new equivalent noise source (I_S') and noise source impedance (Z_S') is given by (3) and (4), respectively. Now, the open-loop current gain ($G_{\rm OL}$) without the active EMI filter is given by (5).

$$V_S = I_S Z_S \tag{1}$$

$$V_{\text{SEN}} = V_S - I_{SA} Z_S = Z_S (I_S - I_{SA})$$
 (2)

$$I_S' = \frac{Z_S}{Z_S + Z_{DM}} I_S \tag{3}$$

$$Z_S' = Z_S + Z_{\rm DM} \tag{4}$$

$$G_{\text{OL}} = \frac{I_{SL}}{I_S'} = \frac{Z_S'}{Z_S' + Z_L} = \frac{Z_S + Z_{\text{DM}}}{Z_S + Z_{\text{DM}} + Z_L}$$
 (5)

The noise source voltage $V_{\rm SEN}$ is sensed by the active EMI filter using a high-pass filter. The output of the high-pass filter $V_{\rm HPF}$ is then inputted to the compensation stage. The output of the compensation stage is $V_{\rm COMP}$ is then used as the noise source V_{St} to the twin circuit. Let $G_{\rm INJ}$ be the ratio of the $V_{\rm INJ}$ to $V_{\rm SEN}$. The injected cancellation current I_{SC} is given by (6). Substituting for $V_{\rm SEN}$ in (6), results in (7).

$$I_{SC} = \frac{I_{SL} Z_{\text{LISN}} + G_{\text{INJ}} V_{\text{SEN}}}{Z_{\text{INJ}}} \tag{6}$$

$$I_{SC} = \frac{I_{SL}Z_{LISN} + G_{INJ}(V_S - (I_{SL} + I_{SC})Z_S)}{Z_{INJ}}$$
 (7)

The twin circuit comprises of feedback control based voltagesense current-cancellation active EMI filter circuit. The detailed derivation of the topology used in the twin circuit is presented in [14] and general current-injection based active EMI filter topologies for DM noise are discussed in detail [10], [15], [16]. So, only final equations are given here for the sake of brevity. The block diagram of the twin circuit is shown in Fig. 5. The circuit schematic and the equivalent circuit of the twin circuit are shown in Fig. 6(a) and (b), respectively. The noise voltage source in the twin circuit is V_{St} . The current through $L_{\rm DMt}$ is I_{SLt} , and the cancellation current is I_{SCt} and the current through $Z_{\rm LISNt}$ is given by I_{SLt} . The feedback gain of the active circuit is represented by A_{jt} . The feedforward current gain and the loop

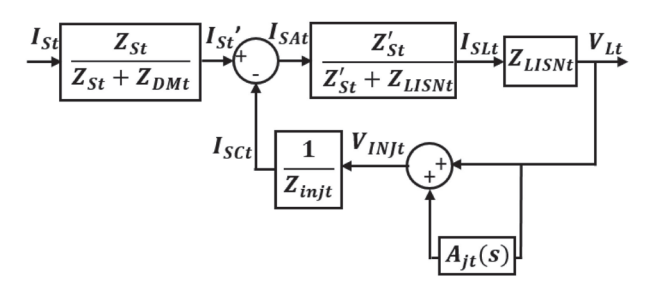


Fig. 5. Block diagram of twin circuit—feedback voltage-sense current-cancellation topology.

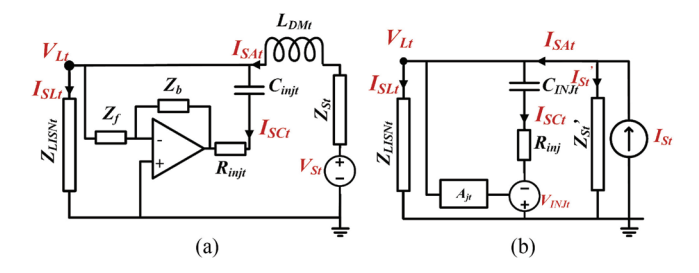


Fig. 6. Equivalent circuit of twin circuit with noise source represented. (a) Voltage source. (b) Current source.

gain of the feedback loop is given in (8) and (9), respectively.

$$\frac{I_{SLt}}{I'_{St}} = \frac{G_t}{1 + G_t \frac{Z_{\text{LISNt}}}{Z_{\text{INJt}}} (1 + A_{jt})}$$
where $G_t = \frac{Z_{\text{DMt}}}{Z_{\text{DMt}} + Z_{\text{LISNt}}}$

$$\frac{V_{\text{INJt}}}{V_{St}} = \frac{I_{SLt}}{I'_{St}} \frac{Z_{\text{LISNt}}}{Z_{\text{DMt}}} A_{jt} \tag{9}$$

Substituting (8) in (9), gives (10).

$$\frac{V_{\rm INJt}}{V_{St}} = \frac{A_{jt}}{\frac{1}{G_t} \frac{Z_{\rm INJt}}{Z_{\rm IJSNt}} + 1 + A_{jt}} \frac{Z_{\rm INJt}}{Z_{\rm DMt}}$$
(10)

The attenuation with the active EMI filter with the twin circuit is then given by (11).

$$G_{CL} = 1 - \frac{V_{\text{INJt}}}{V_{St}} \frac{Z_{\text{DM}}}{Z_{\text{INJt}}} T_{\text{HPF}} T_{\text{COMP}}$$

$$G_{CL} = 1 - \frac{A_{jt}}{\frac{1}{G_t} \frac{Z_{\text{INJt}}}{Z_{\text{INSN}}} + 1 + A_{jt}} \frac{Z_{\text{INJt}}}{Z_{\text{DMt}}} \frac{Z_{\text{DM}}}{Z_{\text{INJ}}}$$

$$(11)$$

$$T_{\rm HPF} T_{\rm COMP}$$
 (12)

Substituting (10) in (11), yields (12). From (12), it can be seen that the attenuation of the proposed filter is highest when the second term is unity. For this to occur, the following conditions need to be satisfied:

- 1) the gain of the twin circuit which in turn determines the ratio of V_{INJt} to V_{St} ;
- 2) the degree to which there is a good match between $Z_{\rm INJ}$ and $Z_{\rm INJt}, Z_{\rm DM},$ and $Z_{\rm DMt};$
- 3) $T_{\rm HPF}T_{\rm COMP}$ should be unity in the EMI frequency range. Furthermore, the attenuation does not depend on the accurate match between $Z_{\rm LISN}$ and $Z_{\rm LISNt}$, which makes the filter more

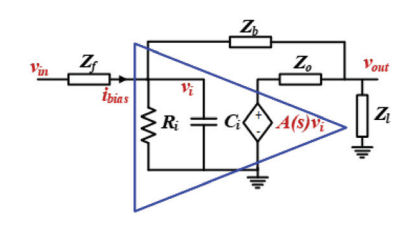


Fig. 7. Schematic of simplified model of op-amp.

robust to noise source impedance variations. The component selection, modeling, and design of each subcircuit and overall circuit design to achieve maximum attenuation with the proposed active EMI filter are discussed next.

A. Operational Amplifier

The proposed active EMI filter uses op-amps in four parts of the circuit. Ideally, all four op-amps could be integrated into one single IC. The first three op-amps are all small signal circuits and do not need The open-loop gain and the output impedance of the op-amp are available in the datasheet [24]. The values from the datasheet are verified by measurements using the VNA. The open-loop gain and the output impedance of the op-amp is measured by configuring it at a known value of closed-loop gain[25]. The simplified model of the op-amp is shown in Fig. 7. The transfer function of the open-loop gain of the op-amp is given by 13. The open-loop gain is around 65 dB at 100 Hz and is capable of supplying up to 75 mA of current. This op-amp is overdesigned to be used as the buffer for the noise sensing and compensation stages. However, for the simplicity of modeling, the same op-amp is used in all three stages.

$$G_{\rm amp} = \frac{G_o}{(1 + s/\omega_1)(1 + s/\omega_2)} \tag{13}$$

where, G_o is the open-loop gain at dc, and ω_1 and ω_2 represent the gain rollover frequencies. $G_o=1780, \omega_1=2\times 180\ krad/s$, and $\omega_2=2\times 350\ Mrad/s$.

B. High-Pass Filter

The converter that uses this filter could be fed from ac or dc supply. Either way, the noise-sensing stage has to sufficiently attenuate any 60 Hz ac voltage its harmonics, and the high-frequency currents due to rectifier operation or any other converters connected to the same node. Otherwise, any low-frequency harmonics can easily saturate the output of the active circuits. Ideally, the output of the high-pass filter should only include the switching frequency and its harmonics in the desired EMI frequency range (150 kHz to few MHz). The design of the sensing network requires careful consideration to ensure that it

- 1) has the desired performance throughout the entire frequency range;
- 2) does not add too much to the volume of the filter.

It is not possible to get around 80 dB attenuation at 60 Hz with a first order high-pass filter. Therefore, a second order high-pass filter is used as the sensing network. The capacitor C_{s1} needs

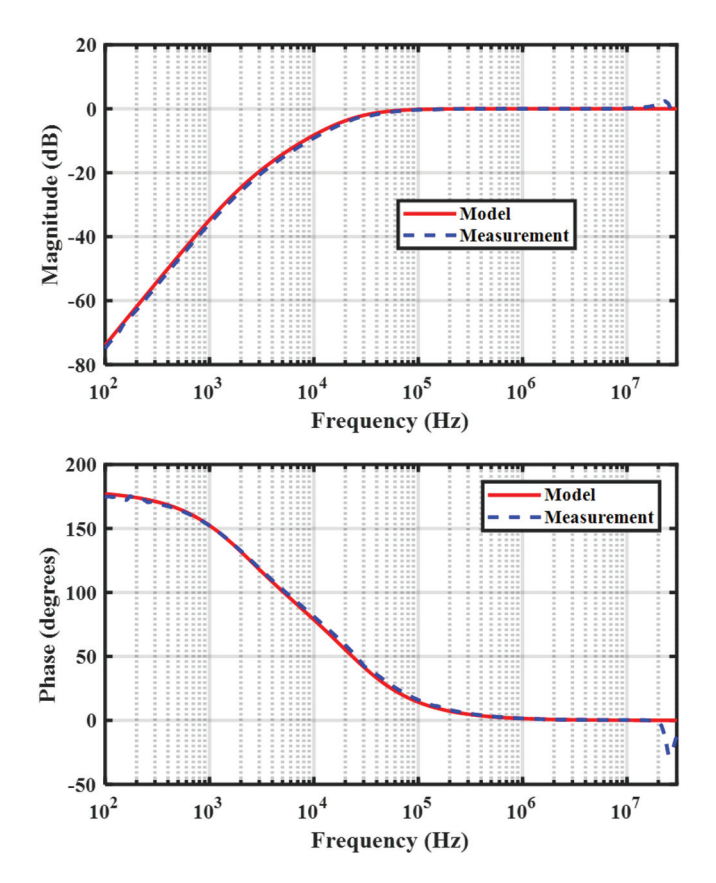


Fig. 8. Frequency response of high-pass filter for noise-sensing—model versus measurement.

to be rated for the input voltage and needs to be safety rated (X1Y1 rated). The other components C_{s2} , R_{s1} , and R_{s2} are low voltage and low-power components. The capacitor C_{s2} is a 50 V rated X7R surface mount capacitor. The transfer function of the filter is given by (14). The output of the high-pass filter is buffered (op-amp configured as voltage follower) and fed to the compensation stage. The selected op-amp is unity-gain stable with a gain-bandwidth of about 500 MHz. Therefore, the output of the buffer could be assumed to be the same as that of the high-pass filter. The transfer function of the filter and the buffer is measured for $C_{s1}=4.7~{\rm nF}, C_{s2}=10~{\rm nF}, R_{s1}=3.3~{\rm k}\Omega$, and $R_{s2}=3.3~{\rm k}\Omega$ using the Bode-100 VNA. The comparison of model and measurement is shown in Fig. 8.

$$T_{\text{HPF}} = \frac{s^2}{s^2 + s(\frac{1}{C_{s1}R_{s1}} + \frac{1}{C_{s1}R_{s2}} + \frac{1}{C_{s2}R_{s2}}) + \frac{1}{C_{s1}C_{s2}R_{s1}R_{s2}}}$$
(14)

C. Compensation

The low-frequency compensation is a lead-lag compensator. As a whole, the proposed analog-twin based active EMI filter is a feedforward implementation. Therefore, the attenuation is maximum when the gain is unity with no phase shift. The high-pass filter that is used to sense the noise reduces the gain and introduces phase shift up to a few 100 kHz. In order to reduce this, a pole-zero pair (lead-lag compensator) is introduced after the high-pass filter. This transfer function of the sensed noised with

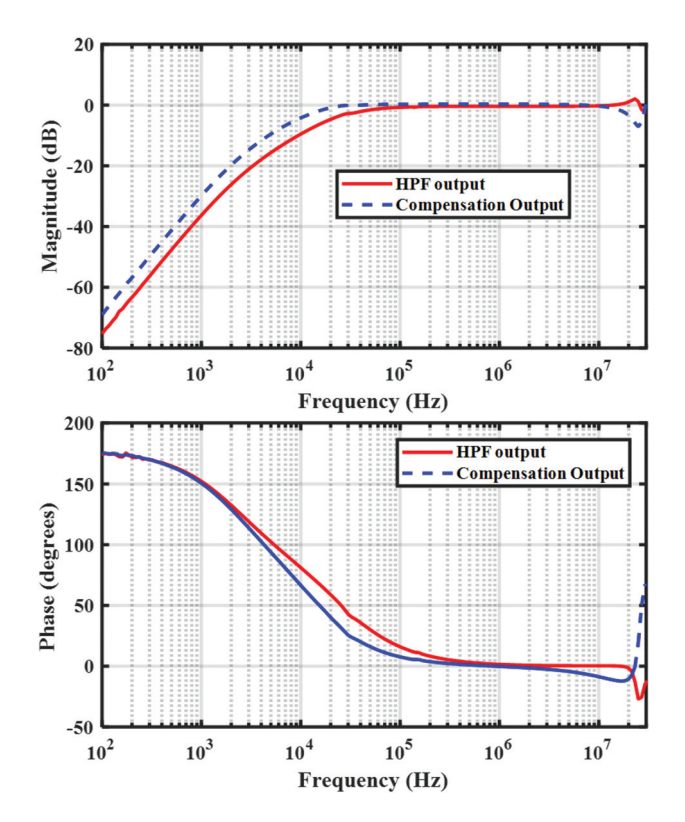


Fig. 9. Frequency response of high-pass filter output with and without compensation.

and without compensation is illustrated in Fig. 9. The lead-lag compensator is chosen such to reduce the distortion in gain and phase in the EMI frequency range without overshooting the gain above unity. The compensation stage consists of a noninverting amplifier with a gain of (2). Since the gain bandwidth (GBW) of the op-amp is of the order of 500 MHz, the transfer function of the op-amp can be assumed to be approximately given by (15). The output of this circuit is fed to the compensation network. The compensation network consists of R_{c1} , R_{c2} , and C_{c1} and is used to introduce a pole-zero pair (lead-lag compensation) around 150 kHz to improve the gain and the phase distortion introduced by the noise-sensing stage. The transfer function of the compensation stage is determined by the noninverting amplifier and the passive network. The transfer function of the compensation network and the noninverting amplifier is given by (16). The transfer function of the filter and the buffer is measured for $C_{c1}=47$ nF, $R_{c1}=120~\Omega,$ and $R_{c2}=120~\Omega$ using the Bode-100 VNA. The comparison of model and measurement is shown in Fig. 8, and the comparison of the sensing stage with and without compensation is shown in Fig. 9. And, comparison of model and measurement of high pass filter with compensation is shown in Fig. 10.

$$T_A = \frac{1 + \frac{R_2}{R_1}}{1 + \frac{1 + (R_2/R_1)}{G_{\text{core}}}} \approx 2 \tag{15}$$

$$T_{\text{COMP}} = \frac{\frac{1}{sC_{c1}} + R_{c2}}{R_{c1} + \frac{1}{sC_{c1}} + R_{c2}} T_A$$
 (16)

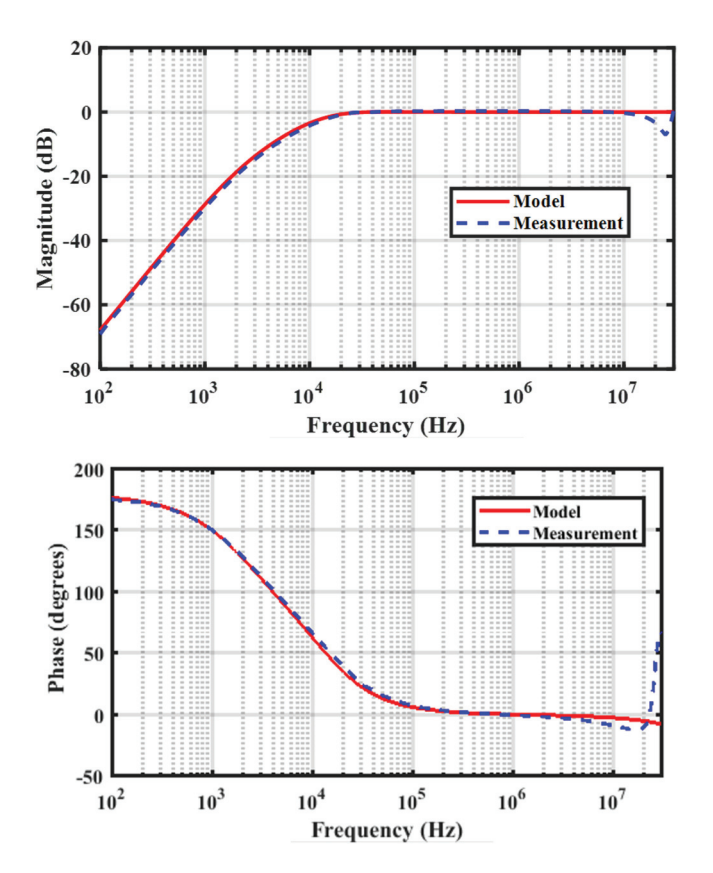


Fig. 10. Frequency response of compensation stage and high-pass filter—model versus measurement.

Besides this, all the op-amps require high-frequency compensation to avoid instability. This is ensured by conventional lag compensation by using a small capacitor across the feedback resistor to reduce the gain at frequencies higher than 30 MHz.

D. Twin Circuit

The twin circuit comprises of feedback control based voltagesense current-cancellation active EMI filter circuit. The detailed derivation of the topology used in the twin circuit is presented in [10], [14]. So, only final equations are given here for the sake of brevity. The block diagram of the twin circuit is shown in Fig. 5. The circuit schematic and the equivalent circuit of the twin circuit are shown in Fig. 6(a), and (b), respectively. The noise voltage source in the twin circuit is V_{St} . The current through L_{DMt} is I_{SLt} , and the cancellation current is I_{SCt} and the current through Z_{LISNt} is given by I_{SLt} . The feedback gain of the active circuit is represented by A_{jt} . The feedforward current gain and the loop gain of the feedback loop is given in (8) and (9), respectively.

The twin circuit comprises of feedback voltage-sense current-cancellation topology which is designed based on [14] and only key details are provided here for the sake of brevity. The gain of the inverting amplifier is set using C_f , Z_f , and Z_b to 24 dB in the frequency range of 150 kHz to 1 MHz. The three main components of the twin circuit are $L_{\rm DMt}$, $C_{\rm INJt}$, and $Z_{\rm LISNt}$ which are identical to the components $L_{\rm DM}$, $C_{\rm INJ}$, and $Z_{\rm LISN}$ in the main power circuit. The twin circuit is configured in the

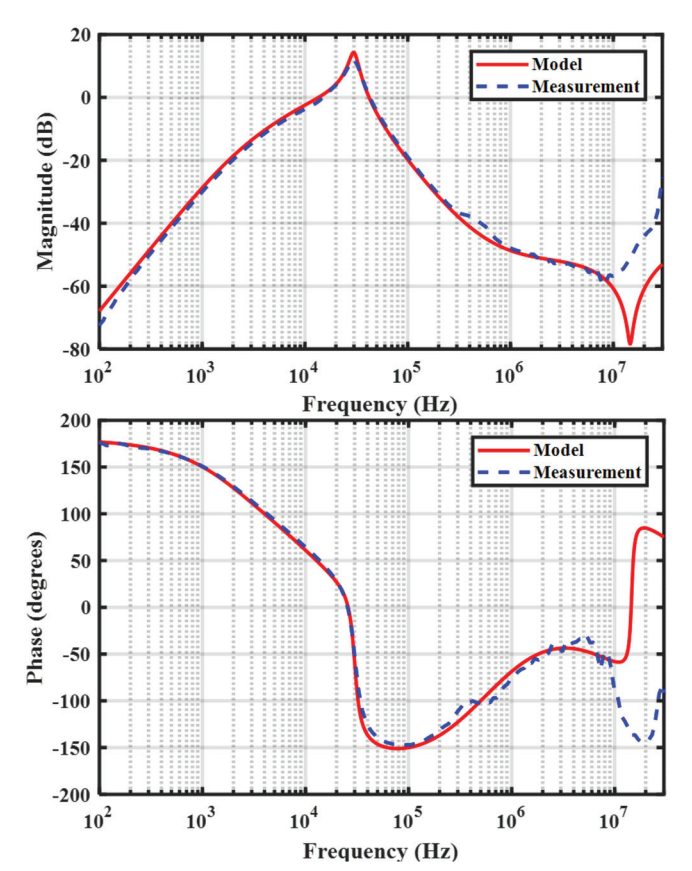


Fig. 11. Frequency domain measurement of $V_{\rm LISNt}$ —model versus measurement.

feedback configuration. It operates to reduce the noise in Z_{LISNt} , which is a 100 Ω resistor. The gain of the amplifier circuit is directly related to the attenuation provided by the active EMI filter. The high-frequency stability of the twin circuit is ensured by using lead-compensation method (adding a capacitor across the feedback resistor) and using an injection resistor in series with C_{INJt} . The loop gain of the twin circuit is given by (17). The gain of the twin circuit is set to ensure that the twin circuit is stable and the output of the op-amp in the twin circuit is not saturated by any low frequency and its harmonics. The voltage $V_{\rm INJt}$ is then fed to a buffer in the injection stage. The output of this buffer is fed to $C_{\rm INJ}$ in the main circuit. The voltages $V_{\rm LISNt}$ and $V_{\rm INJt}$ are measured using the VNA for $L_{DMt}=33~\mu{\rm H}$, $C_{\rm INJt} = 47$ nF, and $Z_{\rm LISNt} = 100 \,\Omega$. The comparison of model and measurement is shown in Figs. 11 and 12 and show good agreement.

$$A_{jt} = T_{IA}(s) \frac{Z_L//Z_S}{(Z_L//Z_S) + Z_{INI}}$$
 (17)

where.

$$\begin{split} T_{IA} &= \frac{G_{\text{op-amp}}(Z_b + (Z_o//Z_l))}{Z_{ff} + Z_b + (Z_o//Z_l)} \frac{1}{1 + G_{\text{op-amp}}\beta} \\ \beta &= \left(\frac{Z_{ff}}{Z_{ff} + Z_b}\right) \left(\frac{Z_l//(Z_{ff} + Z_b)}{Z_l//(Z_{ff} + Z_b) + Z_o}\right) \\ Z_l &= Z_{\text{INJt}} + Z_{\text{LISNt}}//Z_{\text{DMt}} \end{split}$$

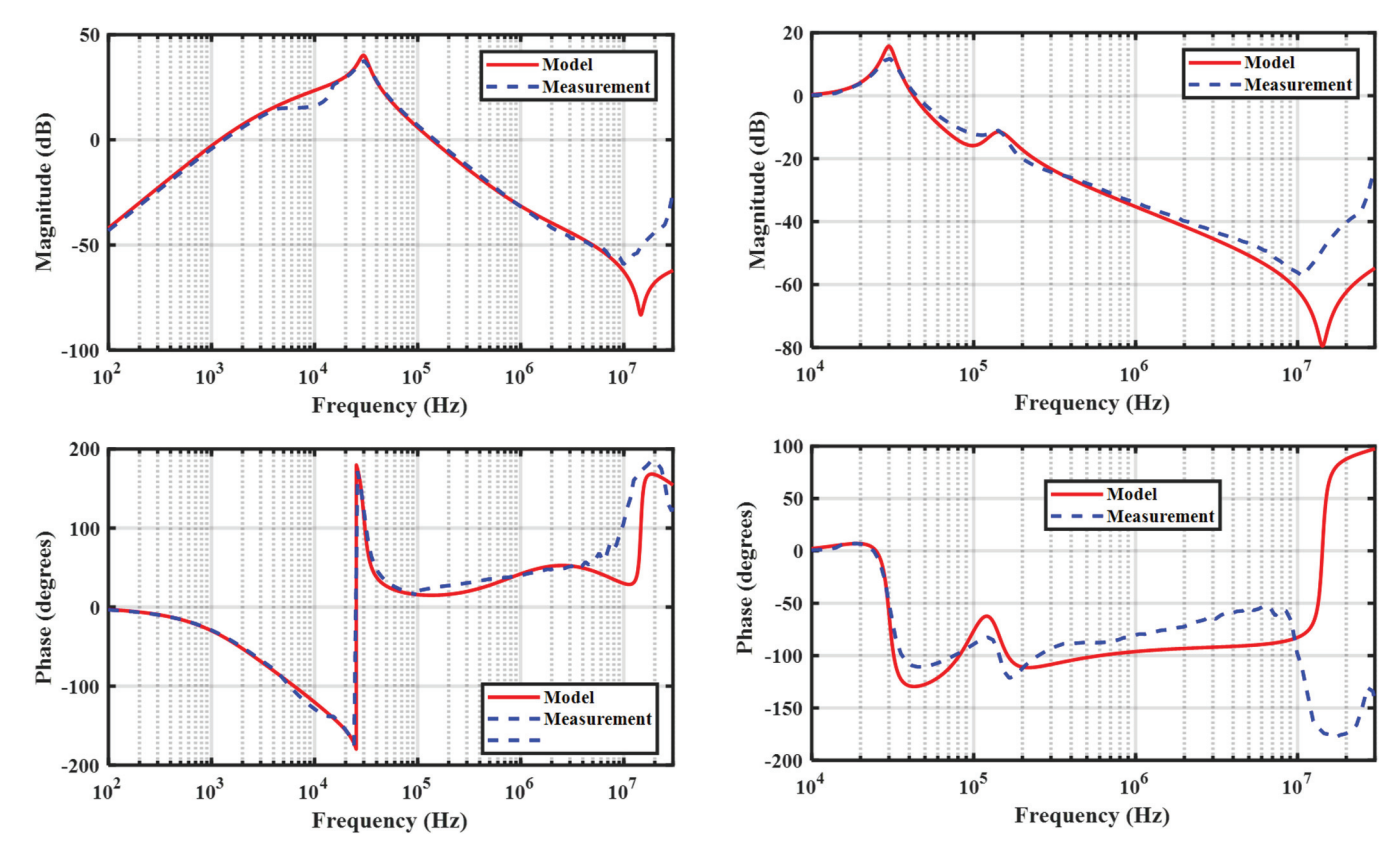


Fig. 12. Frequency domain measurement of $V_{\rm INJt}$ —model versus measurement.

Fig. 13. Insertion loss of analog twin active EMI filter—model versus measurement.

E. Injection Network and Insertion Loss

The V_{INJt} voltage from the twin circuit is buffered and injected in the main circuit using C_{INJ} . A series resistor R_{INJ} is added to damp the resonance between $L_{\rm DM}$ and $C_{\rm DM}$, similar to the twin circuit. The model versus measurement of insertion loss of the proposed analog-twin based active EMI filter is shown in Fig. 13. The measurement shows good agreement to the model up to a few MHz. The comparison of insertion loss with the inductor $L_{\rm DM}$ (33 $\mu \rm H$), passive components $L_{\rm DM}$ (33 $\mu \rm H$), and $C_{\rm DM}$ (47 nF) only, the same passive components, $L_{\rm DM}$ (33 $\mu \rm H)$ and $C_{\rm INJ}$ (47 nF), when used with the analog-twin based active EMI filter, is shown in Fig. 14. In order to see the additional attenuation by the active EMI filter, the value of $C_{\rm DM}$ and $C_{\rm INJ}$ is kept the same. When compared to the passive components only, the active EMI filter provides 24 dB at 150 kHz with the bandwidth of 1 MHz. However, along with $L_{\rm DM}$, the bandwith of the overall hybrid filter encompasses the entire conducted EMI frequency range of CISPR-22 standard (150 kHz to 30 MHz).

IV. EXPERIMENTAL RESULTS

A. Small Signal Test Results

For carrying out the small-signal tests, the function generator is used as the noise source. Since the output of the function generator has a 50 Ω output impedance, the function generator is used with an op-amp configured as a voltage follower. In addition, a 30 μF capacitor in series to the output of the voltage

follower to represent the capacitive noise source impedance in the actual converter. The output through the capacitor is then connected to the active EMI filter, and tests are carried out under two cases. One with the $L_{\rm DM}$ and $C_{\rm DM}$ and another with the $L_{\rm DM}$ and the proposed active EMI filter. The active EMI filter uses C_{INJ} same as that of C_{DM} . The noise is measured at the LISN with a DM noise splitter (minicircuits ZSCJ-2-2+). The output of the DM noise splitter is connected to the Keysight MXE EMI receiver. The time-domain waveforms at different stages of the proposed active EMI filter are measured using TPP1000 1 GHz passive probes and a Tektronix MSO-56 Oscilloscope and shown in Fig. 15. The noise voltage (V_{source}) is sensed using the high-pass filter $(V_{\rm HPF})$ is distorted due to the nonlinear phase shift introduced by the high-pass filter. The output of the compensation network has lower distortion and corresponds well to V_{source} . The injection signal (V_{INJ}) does not have any high frequency or low-frequency ringing confirming that the filter is stable. The frequency-domain measurements from the EMI receiver are shown in Fig. 16. With the proposed active EMI filter, there is about 24 dB attenuation around 150 kHz and the bandwidth of 1 MHz corresponds to the frequency domain measurements using the VNA.

B. Experimental Results With Converter

The measurement setup is the same as that of the small-signal test results. The filter is connected to a buck converter with a switching frequency of 50 kHz and 75% duty cycle. The

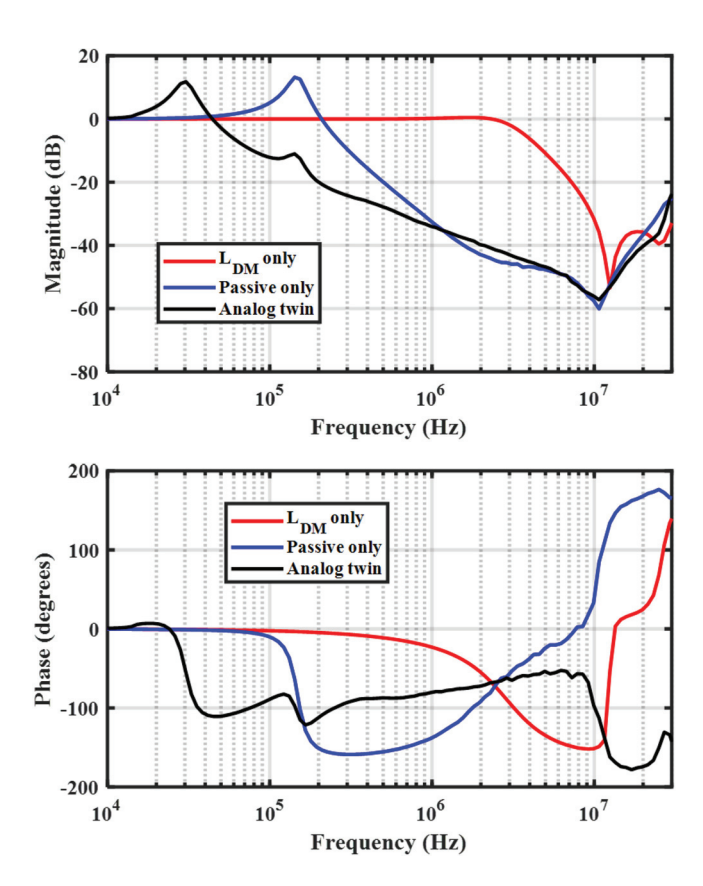


Fig. 14. Measured insertion loss of $L_{\rm DM}=33~\mu H$ only, passive components ($L_{\rm DM}=33~\mu H$ and $C_{\rm DM}=47~{\rm nF}$) only and with analog twin ($L_{\rm DM}=33~\mu H$, $C_{IN,I}=47~{\rm nF}$ and active circuit).

measurements are carried out under the same two cases, as previously mentioned in the small-signal tests. The time-domain measurements and are shown in Fig. 17 and the EMI receiver measurements are shown in Fig. 18, respectively. From Fig. 17, the distortion introduced by the high-pass filter has been corrected by the compensation network. The injection stage has no high-frequency or low-frequency ringing, ensuring that the filter is stable. From Fig. 18, the attenuation at 150 kHz is around 24 dB, which is consistent with the small-signal results and VNA measurement. There is some attenuation up to 1 MHz, which is also consistent with the measurements using the VNA.

C. Power Loss and Volume Reduction

The demonstration of the proposed filter includes three opamps. For simplicity of modeling all the four op-amps were chosen to be same model. Also, as mentioned earlier, all of these op-amps could be integrated into a single op-amp. Therefore, the bias power of only one op-amp is considered for calculation of power loss. All the losses in the op-amp are calculated using 5 V bias power. The quiescent power loss in the op-amp is about 50 mW corresponding to quiescent current of about 10 mA. There are losses in the injection op-amp due to the leakage current in the injection capacitors. For dc systems, this loss is negligible. For ac 110 V 60 Hz supply, the leakage current is about 2 mA (for 47 nF $C_{\rm INJ}$) which translates to about 10 mW in losses in the op-amp. Besides these losses, there is loss due

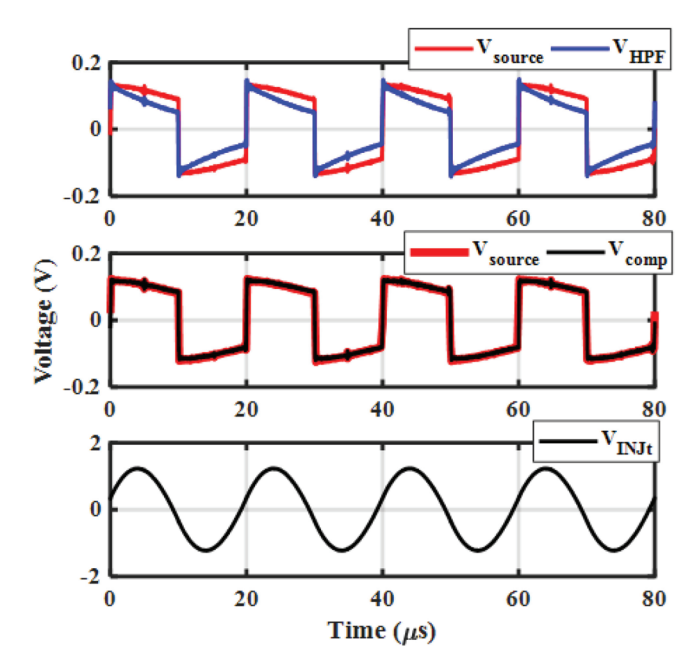


Fig. 15. Small signal time-domain measurements.

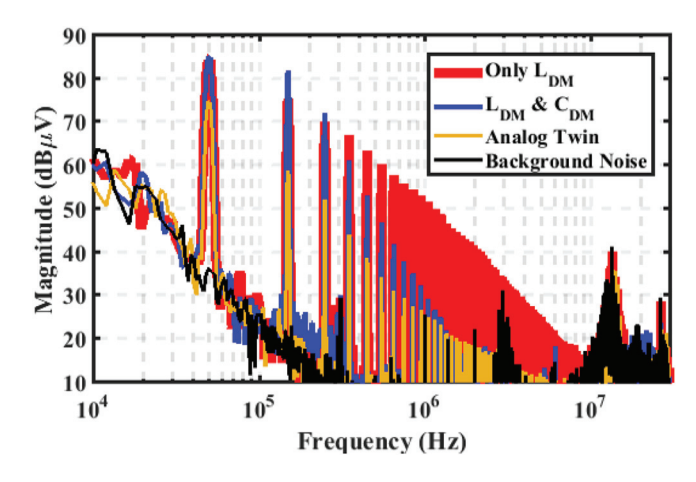


Fig. 16. Small signal frequency-domain measurements with EMI receiver.

to injected current. From Fig. 18, the majority of the injected noise current is only up to 500 kHz. So higher harmonics can be neglected. At 150 kHz, the noise reduces from 66 to 42 dB μ V. These corresponds to 39.9 and 2.5 mA of current measured at the LISN at 150 kHz. Therefore, the losses in the injection op-amp is about 188 mW. Similarly, corresponding to noise injected up to harmonics of 500 kHz, the total power loss due to injection current is about 725 mW. Thus, the total power loss (quiescent + leakage current + injection current) is 785 mW. Majority of the losses comes from due to the noise cancellation current. At 30 W power level, the losses are about 2.5%. However, for the same attenuation, same amount of cancellation-current is injected in the circuit at any power level. For example, consider the case where the analog-twin based active EMI filter is used in 300 W converter. To arrive at worst case estimates, the bias voltage for the amplifiers is assumed to 15 V instead of 5 V. Then, the power losses in incurred in the injection circuit will be 2.175 W, which

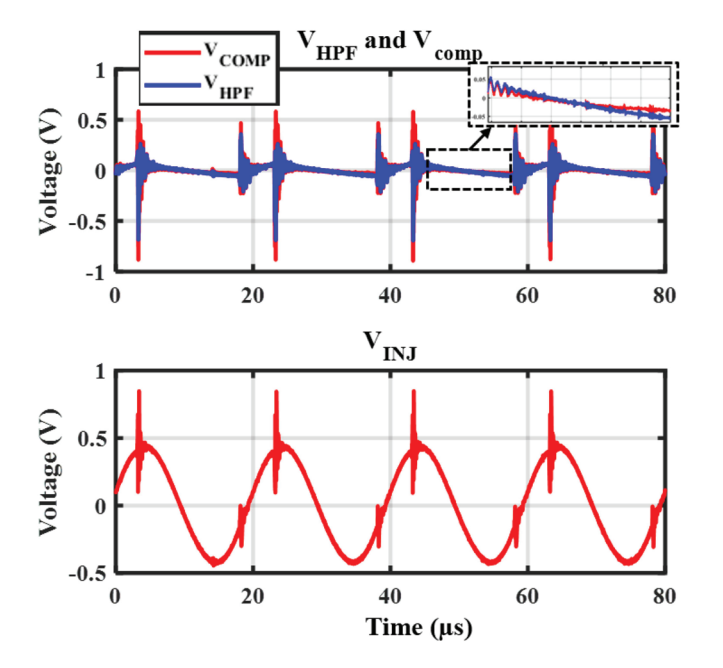


Fig. 17. Time-domain converter test results.

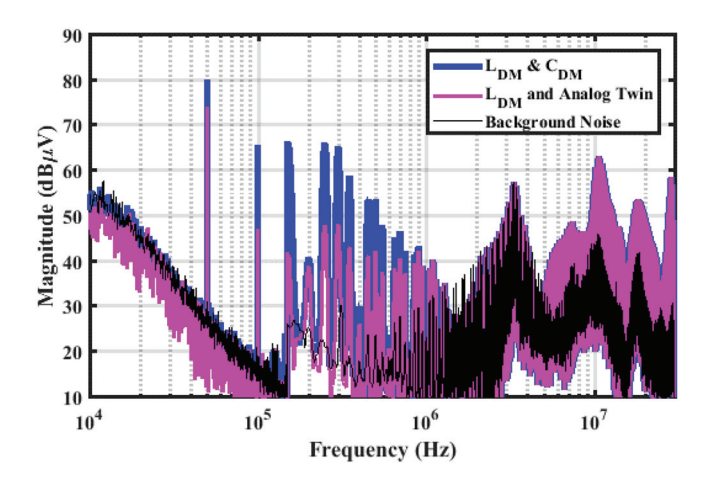


Fig. 18. Converter test frequency-domain measurements with EMI receiver.

corresponds to about 0.7%. Therefore, the percentage of losses incurred in the active EMI filter for the same attenuation reduces as the power level increases. Furthermore, corresponding to a reduction of capacitance (X2, 275 Vac rated) from 470 nF (3790 cu. mm.) to 47 nF (1215 cu. mm.), the volume reduction of required capacitor is about 68%.

V. CONCLUSION

A novel feedforward control based voltage-sense current-cancellation topology with a twin circuit that uses only high-voltage capacitors for noise sensing and cancellation is proposed. The topology uses only low-voltage surface mount components for compensation to improve attenuation and ensure the stability of the active EMI filter. The twin circuit consists of components that are identical to that of the main circuit. The individual subcircuits are modeled in detail to arrive at the overall

system model and insertion loss. The small-signal measurements are carried out using the VNA at the subcircuit level, and system level, and the insertion loss of the proposed filter is compared to the passive filter. The model is in good agreement with the measurement up to a few MHz. The small-signal test results and experimental test results show an attenuation of 24 dB at 150 kHz using a 47 nF capacitor, and a bandwidth of 1 MHz. This would enable replacing a 470 nF capacitor with a 47 nF one using the proposed active EMI filter resulting in a 68% smaller capacitor.

REFERENCES

- [1] Z. Yuan *et al.*, "Design and evaluation of laminated busbar for 3-level T-type NPC power electronics building block with enhanced dynamic current sharing," *IEEE J. Emerg. Sel. Topics Power Electron.*, vol. 8, no. 1, pp. 395–406, Mar. 2020.
- [2] A. Deshpande, Y. Chen, B. Narayanasamy, Z. Yuan, C. Chen, and F. Luo, "Design of a high efficiency, high specific-power three-level T-type power electronics building block for aircraft electric-propulsion drives," *IEEE J. Emerg. Sel. Topics Power Electron.*, vol. 8, no. 1, pp. 407–416, Mar. 2020.
- [3] H. Peng, Z. Yuan, B. Narayanasamy, X. Zhao, A. Deshpande, and F. Luo, "Comprehensive analysis of three-phase three-level T-type neutral-pointclamped inverter with hybrid switch combination," in *Proc. IEEE 10th Int.* Symp. Power Electron. Distrib. Gener. Syst., Jun. 2019, pp. 816–821.
- [4] H. Peng et al., "Improved space vector modulation for neutral-point balancing control in hybrid-switch-based T-type neutral-point-clamped inverters with loss and common-mode voltage reduction," CPSS Trans. Power Electron. Appl., vol. 4, no. 4, pp. 328–338, 2019.
- [5] Y. Chen, A. S. Sathyanarayanan, B. Narayanasamy, W. Feng, and F. Luo, "Comprehensive evaluation of interleaved zero current switching inverter against interleaved hard switching inverters in terms of efficiency, power density and EMI spectrum," in *Proc. IEEE Appl. Power Electron. Conf. Expo.*, 2017, pp. 2253–2258.
- [6] A. I. Emon, B. Narayanasamy, T. M. Evans, F. Luo, and H. A. Mantooth, "Modeling and analysis of near-field radiated emission in wide bandgap power modules," in *Proc. Int. Symp. Electromagn. Compat.*, 2019, pp. 333–338.
- [7] T. Evans, Y. P. F. L. Q. Le, B. Narayanasamy, and H. Mantooth, "Development of EDA techniques for power module EMI modeling and layout optimization," in *Proc. Int. Symp. Microelectron.*, 2019, pp. 193–198.
- [8] J. Biela, A. Wirthmueller, R. Waespe, M. L. Heldwein, K. Raggl, and J. W. Kolar, "Passive and active hybrid integrated EMI filters," *IEEE Trans. Power Electron.*, vol. 24, no. 5, pp. 1340–1349, May 2009.
- [9] M. Ali, E. Labour, and F. Costa, "Integrated active filter for differential-mode noise suppression," *IEEE Trans. Power Electron.*, vol. 29, no. 3, pp. 1053–1057, Mar. 2014.
- [10] R. Goswami, S. Wang, E. Solodovnik, and K. J. Karimi, "Differential mode active EMI filter design for a boost power factor correction AC/DC converter," *IEEE J. Emerg. Sel. Topics Power Electron.*, vol. 7, no. 1, pp. 576–590, Mar. 2019.
- [11] S. Wang, Y. Y. Maillet, F. Wang, D. Boroyevich, and R. Burgos, "Investigation of hybrid EMI filters for common-mode EMI suppression in a motor drive system," *IEEE Trans. Power Electron.*, vol. 25, no. 4, pp. 1034–1045, Apr. 2010.
- [12] Y. C. Son and S.-K. Sul, "Generalization of active filters for EMI reduction and harmonics compensation," *IEEE Trans. Ind. Appl.*, vol. 42, no. 2, pp. 545–551, Mar./Apr. 2006.
- [13] N. K. Poon, J. C. P. Liu, C. K. Tse, and M. H. Pong, "Techniques for input ripple current cancellation: Classification and implementation [in smps]," *IEEE Trans. Power Electron.*, vol. 15, no. 6, pp. 1144–1152, Nov. 2000.
- [14] B. Narayanasamy, F. Luo, and Y. Chu, "Modeling and stability analysis of voltage sensing based differential mode active EMI filters for AC–DC power converters," in *Proc. IEEE Symp. Electromagn. Compat., Signal Integrity Power Integrity*, Jul. 2018, pp. 322–328.
- [15] R. Goswami and S. Wang, "Modeling and stability analysis of active differential-mode EMI filters for AC/DC power converters," *IEEE Trans. Power Electron.*, vol. 33, no. 12, pp. 10 277–10 291, Dec. 2018.
- [16] R. Goswami and S. Wang, "Investigation and modeling of combined feedforward and feedback control schemes to improve the performance of differential mode active EMI filters in AC–DC power converters," *IEEE Trans. Ind. Electron.*, vol. 66, no. 8, pp. 6538–6548, Aug. 2019.

- [17] B. Narayanasamy, F. Luo, and Y. Chu, "High density EMI mitigation solution using active approaches," in *Proc. IEEE Int. Symp. Electromagn. Compat. Signal/Power Integrity*, 2017, pp. 813–818.
- [18] P. Pairodamonchai, S. Suwankawin, and S. Sangwongwanich, "Design and implementation of a hybrid output emi filter for high-frequency commonmode voltage compensation in PWM inverters," *IEEE Trans. Ind. Appl.*, vol. 45, no. 5, pp. 1647–1659, Sep./Oct. 2009.
- [19] D. Shin, S. Jeong, and J. Kim, "Quantified design guidelines of a compact transformerless active EMI filter for performance, stability, and high voltage immunity," *IEEE Trans. Power Electron.*, vol. 33, no. 8, pp. 6723–6737, Aug. 2018.
- [20] Y. Chu, S. Wang, and Q. Wang, "Modeling and stability analysis of active/hybrid common-mode EMI filters for dc/dc power converters," *IEEE Trans. Power Electron.*, vol. 31, no. 9, pp. 6254–6263, Sep. 2016.
- [21] M. L. Heldwein, H. Ertl, J. Biela, and J. W. Kolar, "Implementation of a transformerless common-mode active filter for offline converter systems," *IEEE Trans. Ind. Electron.*, vol. 57, no. 5, pp. 1772–1786, May 2010.
- [22] B. Narayanasamy and F. Luo, "A survey of active EMI filters for conducted EMI noise reduction in power electronic converters," *IEEE Trans. Electromagn. Compat.*, vol. 61, no. 6, pp. 2040–2049, Dec. 2019.
- [23] B. Narayanasamy and F. Luo, "Design and implementation of a novel differential mode active EMI filter with a twin circuit," in *Proc. IEEE Int. Symp. Electromagn. Compat., Signal Power Integrity*, Jul. 2019, pp. 241–246.
- [24] Texas-Instruments, *OPA656 Wideband, Unity-Gain Stable, FET-Input Oper. Amplifier*, 2015. [Online]. Available: http://www.ti.com/lit/ds/symlink/opa656.pdf
- [25] O-Micron, "Application note-Open loop gain of operational amplifiers using Bode-100 VNA," 2018. [Online]. Available: https://www.omicron-lab.com/fileadmin/assets/Bode_100/ApplicationNote s/Op-Amp_Analysis/2018-01-18_Appnote_open_loop_gain_V1.1.pdf



Balaji Narayanasamy (Member, IEEE) received the bachelor's degree in electrical and electronics engineering from Amrita University, Coimbatore, India, in 2012, and the master's degree in electrical engineering from The Ohio State University, Columbus, OH, USA, in 2016. He is currently working toward the Ph.D. degree in electrical engineering with the University of Arkansas, Fayetteville, AR.

Before joining his master's degree, he worked as an Executive Engineer with L&T Kobelco Machinery, India, from 2012 to 2014. He has authored and

coauthored 15 conference and five journal publications. His current research interests include analysis and mitigation of EMI using high density passive and active EMI filters and wide-bandgap devices based power converters.



Zhao Yuan received the B.S. degree from the Huazhong University of Science and Technology, Wuhan, China and the master's degree from Arizona State University, Tempe, AZ, USA, in 2015 and 2017, respectively, both in electrical engineering. He is currently working toward the Ph.D. degree in electrical engineering with the University of Arkansas, Fayetteville, AR.

He is currently a Graduate Researching Assistant involved in the research project with the National Science Foundation Engineering Research Center for

Power Optimization of Electro-Thermal Systems. In 2019, he was a research intern with United Technologies Research Center, East Hartford, CT. His current research interests include design and electro-thermal optimization of high-power converters for traction systems, power module packaging, as well as analysis and mitigation of EMI in wide-bandgap devices-based power converters.

Mr. Yuan was the recipient of Second Place Student Paper Award at the 2018 National Aerospace & Electronics Conference.



power application.

Asif Imran Emon (Graduate Student Member, IEEE) was born in Chittagong, Bangladesh, in 1993. He received the B.Sc. degree in electrical and electronic engineering from the Chittagong University of Engineering and Technology, in 2015. He is currently working toward the Ph.D. degree in electrical engineering with the University of Arkansas, Fayetteville, AR, USA.

His current research interests include power module packaging of wide-band gap devices, and electromagnetic interference and compatibility in high-



Hongwu Peng (Graduate Student Member, IEEE) received the B.S. degree in electrical engineering from the Huazhong University of Science and Technology, Wuhan, China, in 2018. He is currently working toward the Ph.D. degree in electrical engineering with the University of Arkansas at Fayetteville, Fayetteville, AR, USA.

His current research interests include highefficiency motor drive with wide-bandgap devices and active EMI cancellation.



Fang Luo received the bachelor's and Ph.D. degrees in electrical engineering from the Huazhong University of Science and Technology, Wuhan, China, in 2003 and 2010, respectively.

He is currently an Assistant Professor with the University of Arkansas, Fayetteville, AR, USA. From 2007 to 2010, he was a joint Ph.D. student with the Center for Power Electronics Systems (CPES), Virginia Tech, supported by the Chinese Scholarship Council and CPES. From 2010 to 2014, he was with CPES, Virginia Tech, first as a Postdoctoral

Researcher and then as a Research Scientist. From 2014 to 2017, he was a Research Assistant Professor with The Ohio State University. In July 2017, he joined the University of Arkansas as a Tenure Track Assistant Professor. His research interests include turbo electric propulsion converters, high-power density converter design, high-density electromagnetic interference filter design, and power module packaging/integration for wide-bandgap devices.